A General Approach to the Linear Stability of Thin Spreading Films

Jeffrey M. Davis, Benjamin J. Fischer, and Sandra M. Troian

Microfluidic Research & Engineering Laboratory (MREL), Department of Chemical Engineering, Princeton University, Princeton NJ 08544-5263, USA

Abstract. Marangoni and thermocapillary driven systems represent two classes of flows in which the variation in surface tension at the gas-liquid interface can generate spontaneously spreading films. This article considers the linear stability of such flows within the lubrication approximation. Since the base state or unperturbed solutions in both cases involve spatially inhomogeneous profiles, the linearized disturbance operators are non-normal and the stability analysis must therefore be generalized beyond a simple modal decomposition. The utility of this type of analysis is first demonstrated for autonomous operators by an example involving thermocapillary spreading subject to a constant thermal gradient. Extension of this non-modal analysis to systems involving non-autonomous operators is demonstrated by an example of Marangoni spreading induced by film contact with an insoluble surfactant monolayer.

1 Introduction

The growing focus on microscale flow phenomena and their extension to microfluidic devices has generated renewed interest in interfacial hydrodynamics and especially in free surface lubrication flows, *i.e.*, flows for which the height to length ratio is exceedingly small. In this limit, liquid systems can sustain an enormous surface to volume ratio. Forces arising from van der Waals interactions, capillarity, thermocapillarity or Marangoni stresses, all of which are usually neglected in large scale flows, dominate the spreading behavior.

Coating flows constitute an important branch of lubrication hydrodynamics in which thin liquid films are made to coat a dry or prewetted substrate by use of body or shear forces. Gravity, centrifugation, or an external gas stream provide the driving forces for falling [18], spin-coated [12,31] or so-called "blown" films [25]. Spreading can also be induced through modulation of the surface tension, which decreases with temperature or surfactant concentration. Gradients in surface tension generate shear stresses at a liquid-vapor interface to produce thermocapillary [26] or Marangoni driven flow [41].

In recent years, numerous experiments have shown that, in many cases, there exists some parameter range for which the liquid film develops instabilities that ultimately destroy the film uniformity. Films driven by gravity, centrifugation or a constant shear stress are observed to develop rivulets at the spreading front as shown in Fig. 1. Multiple unstable fronts can develop in spreading induced by gradients in surfactant concentration, as demonstrated by the images of the cellular and fractal-like instabilities in Fig. 2. The use of surfactants typically

J.M. Davis, B.J. Fischer, and S.M. Troian, A General Approach to the Linear Stability of Thin Spreading Films, Lect. Notes Phys. **628**, 79–106 (2003)
http://www.springerlink.com/

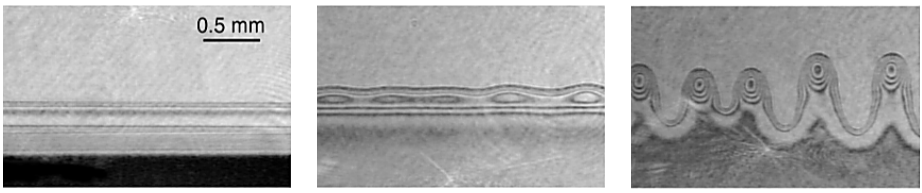

Fig. 1. Thermocapillary spreading of a thin silicone oil film (polydimethyl siloxane) on a differentially heated silicon wafer for $\tau = 0.79$ dyn/cm^2. Spreading proceeds from warmer to cooler regions of the substrate. Optical interference fringes indicate a film thickness $h_c \approx 0.56\mu$m. The time interval between images is 10 min.[23]

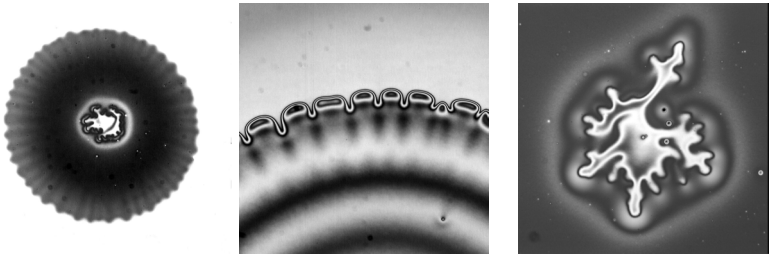

a **b** **c**

Fig. 2. **a** Spreading of a 5 cSt silicone oil (PDMS) droplet on a silicon substrate prewetted with a $0.5 \pm 0.1\mu$m film of pure glycerol 3388 sec after deposition (field of view=9.9mm). **b** Magnified view of a cellular pattern which develops at the border of the spreading droplet (field of view=8.1 mm). **c** Magnified view of a dendritic pattern at the drop center (field of view=2.5 mm). The images do not correspond to the same droplet. Courtesy of Dr. A.A. Darhuber, MREL, Princeton University

results in the ramified structures shown in Fig. 3, which are produced by repeated branching and tip-splitting of moving fronts [42].

This article focuses on thin Newtonian films driven to spread cross a smooth, homogeneous surface through modulation of the liquid surface tension γ, although the analysis can be extended to any of the other flows mentioned above. This modulation, which can be enforced via thermal or concentration gradients, creates shear stresses $\boldsymbol{\tau} = \nabla\gamma$ at the gas-liquid interface that drive liquid from regions of low to high surface tension. In what follows, the linear stability of two systems will be considered: (i) thermocapillary spreading in which a constant shear stress is applied to a liquid film by differentially heating the supporting substrate and (ii) Marangoni spreading in which a non-uniform distribution of insoluble surfactant creates a non-constant shear stress that drives the spreading process.

Within the lubrication approximation [6], the simplified Navier-Stokes equations can be integrated, and the velocity in the film can be found directly from the liquid height profile. The kinematic boundary condition, $\boldsymbol{v} \cdot \hat{n} = D\tilde{h}/Dt$, where D/Dt denotes the material derivative and $\boldsymbol{v}$ the fluid velocity, dictates that the normal component of the surface velocity equal the speed of the gas-

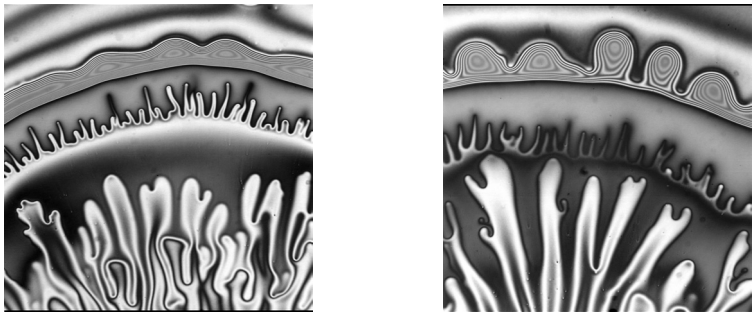

(a) (b)

Fig. 3. Spreading of a glycerol droplet containing sodium dodecyl sulfate (surfactant) on a silicon wafer prewetted with a uniform glycerol layer formed by spin coating at 2000 rpm for 50s at 42% relative humidity. The images show two representative patterns **a** 92 min and **b** 192 min after droplet deposition (field of view = 9.9 mm). The spreading proceeds toward the top of each panel. The black and white contrast is caused by thin film optical interference fringes. Courtesy of Dr. A.A. Darhuber, MREL, Princeton University

liquid interface. Integrating the incompressible form of the continuity equation by parts and using this kinematic condition yields an equation for the film height, $\tilde{h}(\boldsymbol{x}, t)$ [32]:

$$\frac{\partial \tilde{h}}{\partial \tilde{t}} + \nabla \cdot \int_0^{\tilde{h}} \boldsymbol{v} \, \mathrm{d}z = \frac{\partial \tilde{h}}{\partial \tilde{t}} + \nabla \cdot \left[\frac{\tilde{h}^2 \nabla \gamma}{2\mu} - \frac{\tilde{h}^3}{3\mu} \nabla p \right] = 0, \tag{1}$$

where $\hat{z}$ is directed normal to the solid substrate. The term proportional to $\nabla\gamma$ describes the contribution to the liquid flux from thermocapillary or Marangoni stresses. The pressure gradient in the third term $\nabla p \equiv \nabla(-\gamma\nabla^2\tilde{h} + A_0\tilde{h}^{-3})$ derives from capillary forces due to interfacial curvature for $|\nabla\tilde{h}|^2 \ll 1$ and attractive van der Waals interactions where A_o is the Hamaker constant. In thermocapillary driven systems, the viscosity μ of the liquid can vary spatially but variations in liquid density are typically much smaller and can be ignored. Other terms accounting for hydrostatic or streamwise gravitational acceleration, or terms arising from boundary conditions used to remove the well known stress singularity at a moving contact line [17], can easily be incorporated into (1). For example, the governing equation in Sect. 2 contains an additional term reflecting a slip boundary condition at the liquid-solid interface. For systems involving surfactant transport, the equation for $\tilde{h}(\boldsymbol{x}, t)$ must be coupled to a second equation describing the convection and diffusion of surfactant at the air-liquid interface. This coupling gives rise to a space- and time-dependent shear stress as discussed in Sect. 3.

Depending on the forces used to drive the spreading, the base state solutions, $\tilde{h}(\boldsymbol{x}, t)$, assume shapes ranging from constant traveling waves, to self-similar profiles to complex time-dependent waveforms. In all cases, this spatial inhomo-

geneity produces linearized disturbance operators $\mathcal{A}$ which are non-normal and therefore do not commute with their adjoint, *i.e.* $\mathcal{A}\mathcal{A}^\dagger \neq \mathcal{A}^\dagger\mathcal{A}$. While the stability of a normal system for all times t is strictly governed by the eigenspectrum of $\mathcal{A}$, this is not necessarily the case for non-normal systems. It is now widely recognized that the modal spectrum for non-normal operators only determines the asymptotic stability as $t \to \infty$ because the eigenfunctions of such operators are not orthogonal. Eigenvectors separated by a small angle are nearly linearly dependent and can strongly interact. This interaction of such eigenvectors with different decay rates can cause large transient growth, so a more generalized stability analysis is required for finite times. The transition to turbulence in both Couette and plane or pipe Poiseuille flow provides a striking example for which traditional modal analysis fails [38]. Farrell and Ioannou [7,8] have developed a rigorous and generalized stability theory for both autonomous and non-autonomous operators. Implementation of this method to non-autonomous systems with non-trivial time dependence, however, can be computationally prohibitive.

1.1 Linear Stability Theory – Modal Approach

The equations governing the evolution of infinitesimal disturbances are obtained by linearizing the relevant interface equations. Discretization of the linearized system produces a set of equations that can be cast in operator form

$$\frac{\mathrm{d}\boldsymbol{G}}{\mathrm{d}t} = \mathbf{A}\boldsymbol{G}, \tag{2}$$

where $\mathbf{A}(t)$ denotes the linearized disturbance operator and $\boldsymbol{G}(t)$ is a vector that represents the state of the system at time t. The traditional approach to stability proceeds by diagonalizing $\mathbf{A}(t)$ into a matrix whose diagonal elements contain the rank ordered eigenvalues, which is equivalent to assuming an exponential time dependence for $\boldsymbol{G}$. If all the eigenvalues have non-positive real part, then the flow is stable. If the real part of any eigenvalue is positive, the flow is unstable. The eigenvalue with largest, positive real part corresponds to the most dangerous or fastest growing mode whose wavelength can be directly compared with experiment. For normal operators, this procedure yields extremely accurate predictions, as in the Bénard problem [2]. For highly non-normal operators, this method can fail to predict instability altogether, as in the transition to turbulence in bounded shear flows [35]. This failure is due to the fact that the matrix used to diagonalize $\mathbf{A}(t)$ is not unitary and therefore cannot be ignored.

1.2 Generalized Linear Stability Theory

The general solution to (2) is given by

$$\boldsymbol{G}(t) = \boldsymbol{\Phi}_{[t,t_0]}\boldsymbol{G}(t_0), \tag{3}$$

where the propagator or matricant $\mathbf{\Phi}_{[t,t_0]}$, which maps the state of the system at time t_0 to its state at time t, obeys the semigroup property $\mathbf{\Phi}_{[t,s]}\mathbf{\Phi}_{[s,t_0]} = \mathbf{\Phi}_{[t,t_0]}$ and satisfies the matrix differential equation [8]

$$\frac{\mathrm{d}\mathbf{\Phi}_{[t,t_0]}}{\mathrm{d}t} = \mathbf{A}(t)\mathbf{\Phi}_{[t,t_0]}, \quad \mathbf{\Phi}_{[t_0,t_0]} = \mathbf{I}. \tag{4}$$

The matricant can be expressed as a multiplicative integral which is formally defined as [13]

$$\mathbf{\Phi}_{[t,t_0]} = \widehat{\int_{t_0}^{t}} \left[\mathbf{I} + \mathbf{A}(s)ds\right] \equiv \lim_{\delta t \to 0} \prod_{j=1}^{n} \left[\mathbf{I} + \mathbf{A}(t_j)\delta t_j\right], \tag{5}$$

with n $\delta t = (t - t_0)$. If the values of the matrix function $\mathbf{A}(t)$ commute, such that $[\mathbf{A}(t_1), \mathbf{A}(t_2)] = 0 \ \forall \ t_1, t_2 \ \in \ (t_0, t)$, then the propagator reduces to the matrix

$$\mathbf{\Phi}_{[t,t_0]} = \exp\left[\int_{t_0}^{t} \mathbf{A}(s)ds\right]. \tag{6}$$

In general, however, (6) is not a solution to (4), as verified by differentiation [13]. For the case of autonomous operators, $\mathbf{A}$ is independent of t, and (6) reduces further to

$$\mathbf{\Phi}_{[t,t_0]} = \exp\left[\mathbf{A}(t - t_0)\right]. \tag{7}$$

The amplification ratio, σ, of an arbitrary initial perturbation, $\boldsymbol{G}(t_0) \neq \mathbf{0}$, over the time interval $[t_0, t]$ is given by

$$\sigma^2 = \frac{(\boldsymbol{G}(t), \boldsymbol{G}(t))}{(\boldsymbol{G}(t_0), \boldsymbol{G}(t_0))} = \frac{\left(\mathbf{\Phi}_{[t,t_0]}\boldsymbol{G}(t_0), \mathbf{\Phi}_{[t,t_0]}\boldsymbol{G}(t_0)\right)}{(\boldsymbol{G}(t_0), \boldsymbol{G}(t_0))}$$

$$= \frac{\left(\mathbf{\Phi}^{\dagger}_{[t_0,t]}\mathbf{\Phi}_{[t,t_0]}\boldsymbol{G}(t_0), \boldsymbol{G}(t_0)\right)}{(\boldsymbol{G}(t_0), \boldsymbol{G}(t_0))}, \tag{8}$$

where the inner product is computed in the Euclidean norm $\|\cdot\| = (\cdot,\cdot)^{1/2}$ and the adjoint linear operator, $\mathbf{\Phi}^{\dagger}$, is defined by $(\boldsymbol{u}, \mathbf{\Phi}\boldsymbol{v}) = (\mathbf{\Phi}^{\dagger}\boldsymbol{u}, \boldsymbol{v})$ for vectors $\boldsymbol{u}$ and $\boldsymbol{v}$. It then follows that the maximum amplification of a disturbance during the time interval $[t_0, t]$ is given by the square root of the maximum eigenvalue of $\mathbf{\Phi}^{\dagger}_{[t_0,t]}\mathbf{\Phi}_{[t,t_0]}$. The structure that undergoes maximum amplification is the corresponding eigenvector of the composite operator [8].

The base states for thin films driven by a constant shear stress reduce to traveling waves of constant speed. In the frame of reference defined by the traveling wave, $\mathbf{A}$ is *autonomous* and the propagator $\mathbf{\Phi}_{[t,0]}$ reduces to the form (7). Section 2 provides a rigorous formulation of the stability behavior and optimal perturbations for thermocapillary driven spreading. By contrast, the spreading of thin films driven by Marangoni stresses derived from a finite surfactant source gives rise to base states whose shapes are space- and time-dependent. The operator $\mathbf{A}$ is therefore *non-autonomous*. Evaluation of (5) for time-dependent base

states, which must be numerically determined, is computationally challenging. The alternative but less-general approach described in Sect. 3, which reduces the relevant system of equations to an initial value problem, nonetheless allows physical insight into the mechanisms promoting instability. Although this approach prevents identification of so-called optimal perturbations, it offers the flexibility of directly probing critical regions of the flow which are highly susceptible to disturbances.

2 Autonomous Operator – Thermocapillary Spreading

Consider a thin incompressible Newtonian film spreading along a horizontal substrate heated by a constant temperature gradient dT/dx. The liquid film is assumed to be sufficiently thin that hydrostatic pressure is negligible. For small Péclet and Biot numbers, the temperature of the air-liquid interface is identical to the substrate thermal profile. Since the surface tension of a liquid decreases linearly (to a first approximation) with increasing temperature [1], the applied thermal gradient produces a constant shear stress $\tau = d\gamma/dx = (d\gamma/dT)\cdot(dT/dx)$, which drives liquid from warmer to cooler regions [25]. The stress singularity that would otherwise occur at the moving contact line is removed [3] by use of the Greenspan slip condition [16]. Other models can be used to relieve the singularity in thermally driven films including a uniform precursor layer [21,22] and a structured van der Waals film [4]. The Greenspan slip model has also been applied to falling films [5].

There exists an inner region at the front of the spreading film of characteristic length $l = h_c/(3Ca)^{1/3}$, which is obtained by balancing the capillary, thermocapillary and viscous forces controlling the flow [40]. The capillary number is defined by $Ca = \mu U_c/\gamma_o$, where μ is the liquid viscosity (assumed constant for short migration distances), γ_o is the reference surface tension, and $U_c \equiv h_c\tau/2\mu$ is the characteristic flow speed generated by thermocapillary forces. The quantity h_c denotes the characteristic film thickness far from the contact line which can be determined from matching the film thickness to the outer region.

The dimensionless form of (1), extended to include slip at the moving contact line, reduces to

$$h_t - \left(h^2\right)_\chi + \nabla\cdot\left[\left(h^3+\alpha h\right)\nabla\nabla^2 h\right] = 0, \tag{9}$$

where α is the dimensionless slip coefficient, $\nabla \equiv \hat{\chi}\partial_\chi + \hat{\zeta}\partial_\zeta$, and subscripts denote partial differentiation with respect to χ, ζ, or t. The stretched variables in (9) are defined by $\chi = -x/l$, $\zeta = y/l$, $h = \tilde{h}/h_c$, and $t = \tilde{t}/(l/U_c)$. The term $(h^2)_\chi$ arises from the applied thermocapillary stresses, and the term $\nabla\cdot(h^3\nabla\nabla^2 h)$ arises from the capillary pressure induced by surface curvature.

The spreading can be viewed from a reference frame moving at constant speed v_o where $\xi = \chi + v_o t$. The position $\xi = \xi_{CL}(\zeta, t)$ denotes the location of the contact line. For unperturbed flow, this (static) location is given by $\xi = 0$. The boundary conditions used to solve the transformed equation

$$h_t + v_o h_\xi - \left(h^2\right)_\xi + \nabla\cdot\left[\left(h^3+\alpha h\right)\nabla\nabla^2 h\right] = 0, \tag{10}$$

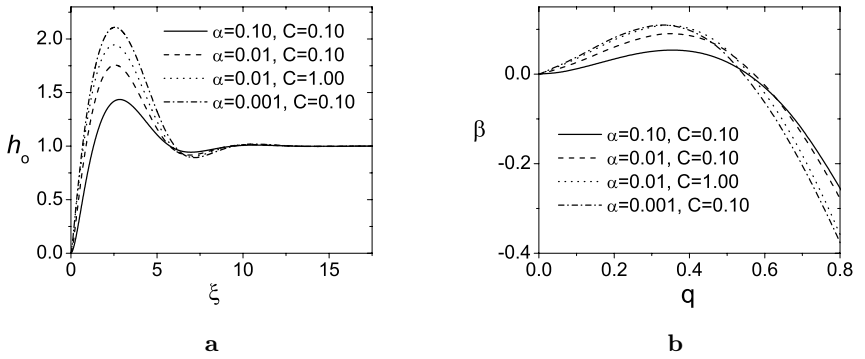

Fig. 4. Numerical solution of **a** the dimensionless, steady state profile, $h_o(\xi)$, and **b** the dispersion curves, $\beta(q)$, obtained from a modal analysis

(where $\nabla \equiv \hat{\xi}\partial_\xi + \hat{\zeta}\partial_\zeta$) are $h(\xi \leq \xi_{CL}) = 0$; $h_\xi(\xi = \xi_{CL}) = \mathsf{C}$, which prescribes the contact angle at the moving front; and $h \to 1$ and $h_{\xi\xi\xi} \to 0$ as $\xi \to +\infty$. The latter two constraints predicate a flat and constant film thickness in matching to the other region.

2.1 Steady Traveling Wave Solutions

The third order equation governing the evolution of the steady base state $h(\xi, \zeta, t) = h_o(\xi)$ is found from integration of (10) to be

$$h_{0\xi\xi\xi} = \frac{h_o - 1}{h_o^2 + \alpha}. \tag{11}$$

The above boundary conditions determine that the wave speed is $v_o = 1$ and that the integration constant vanishes. Equation (11) is converted to a system of first order equations which are solved using a standard shooting method for stiff ODEs. Solutions for different values of the slip coefficient ($0.001 < \alpha < 0.10$) and contact slope ($0.1 < \mathsf{C} < 1.0$) are shown in Fig. 4a. Smaller values of C have only a small influence on the height profile and are not shown. The maximum amplitude of the capillary ridge that develops behind the moving contact line increases with decreasing slip or increasing contact slope.

2.2 Linear Stability of Traveling Waves

Profiles with large capillary ridges as shown in Fig. 4a can undergo sinusoidal fingering instabilities with well defined (dimensionless) wavenumber q (scaled by l) in the transverse direction ($\hat{\zeta}$). Substitution of perturbed waveforms $h(\xi, \zeta, t) = h_o(\xi) + \varepsilon h_1(\xi, \zeta, t)$ with $\varepsilon \ll 1$ into (10), where

$$h_1(\xi, \zeta, t) = G(\xi, t) \exp(iq\zeta), \tag{12}$$

yields the evolution equation for the streamwise disturbance function $G(\xi, t)$:

$$\frac{\partial G}{\partial t} = \left[2h_{o\xi} - \frac{(\alpha + 3h_o^2)(2h_o + \alpha - h_o^2)h_{0\xi}}{(h_o^2 + \alpha)^2} - \alpha q^4 h_o - q^4 h_o^3 - \frac{6h_o h_{0\xi}(h_o - 1)}{h_o^2 + \alpha}\right] G$$

$$+ \left[-1 + 2h_o + 3q^2 h_o^2 h_{0\xi} + \alpha q^2 h_{o\xi} - \frac{(\alpha + 3h_o^2)(h_o - 1)}{h_o^2 + \alpha}\right] G_\xi$$

$$+ \left(2\alpha q^2 h_o + 2q^2 h_o^3\right) G_{\xi\xi} + \left(-\alpha h_{o\xi} - 3h_o^2 h_{o\xi}\right) G_{\xi\xi\xi} + \left(-\alpha h_o - h_o^3\right) G_{\xi\xi\xi\xi} \,. \tag{13}$$

Note that the time dependence of $G(\xi, t)$ is not assumed to have exponential form. Equation (13) is solved subject to four boundary conditions [37]. Two conditions demand that the disturbance decays upon approach to the outer region, *i.e.* $G(\xi \to +\infty) = 0$ and $G_\xi(\xi \to +\infty) = 0$. The third condition follows from the combined Taylor expansions of h and h_ξ about $\xi = \xi_{CL}$:

$$\begin{aligned} h(\xi_{CL}) &\approx h_o(0) + \varepsilon G(0) + \xi_{CL} h_{o\xi}(0) \quad \text{and} \\ h_\xi(\xi_{CL}) &\approx h_{o\xi}(0) + \varepsilon G_\xi(0) + \xi_{CL} h_{o\xi\xi}(0), \end{aligned} \tag{14}$$

where terms of order $\varepsilon\xi_{CL}$ are neglected. Combining these results with the boundary conditions $h(\xi_{CL}) = h_o(0) = 0$ and $h_\xi(\xi_{CL}) = h_{o\xi}(0) = \mathsf{C}$ yields one boundary condition for the disturbance at $\xi = 0$:

$$h_{o\xi\xi} G - \mathsf{C} G_\xi = 0. \tag{15}$$

The second condition at $\xi = 0$ is obtained by evaluating (13) at the contact line (where $h_o = 0$) and using (15):

$$G_t - \left(\mathsf{C} + \alpha q^2 h_{o\xi\xi}\right) G + \alpha \mathsf{C} G_{\xi\xi\xi} = 0. \tag{16}$$

2.3 Asymptotic Behavior

The asymptotic stability of a non-normal system in the limit $t \to \infty$ is determined from the modal spectrum [7]. In this limit, solutions to (13) can be further specified according to $G(\xi, t) = H(\xi)\exp(\beta t)$, where β denotes the disturbance growth rate. The numerical solutions were obtained by discretizing (13) using a central difference scheme and using a standard QR algorithm for calculating the relevant eigenvalues and eigenfunctions. The dispersion curves, $\beta(q)$, corresponding to the four base state height profiles shown in Fig. 4a are plotted in Fig. 4b. There exists a band of unstable wavenumbers in the range $0 < q \leq 0.5$ with maximum growth rate at $q_{\max} \approx 0.35$. The growth rate with $\alpha = 0.01$ and $\mathsf{C} = 1.00$ is nearly as large as that obtained with $\alpha = 0.001$ and $\mathsf{C} = 0.10$. The value $\beta(q_{\max})$ increases as the slip coefficient decreases or the contact slope increases. This behavior confirms that the higher the capillary ridge, the more unstable the flow.

2.4 Optimal Amplification Ratio

Equation (13) can be represented in the form (2), where the autonomous matrix $\mathbf{A}$ contains the elements obtained from the discretization of the linearized equation. The matrix is real, square, banded, nondefective and non-normal. The formal solution to (2) then reduces to the operator exponential acting on the initial condition $\boldsymbol{G}_o$:

$$\boldsymbol{G}(t) = \exp(t\mathbf{A})\boldsymbol{G}_o. \tag{17}$$

It follows that the maximum possible amplification over time t is given by

$$\sigma_{\max}(t) \equiv \sup_{\boldsymbol{G}_o \neq 0} \frac{\|\boldsymbol{G}\|}{\|\boldsymbol{G}_o\|} = \|\exp(t\mathbf{A})\|. \tag{18}$$

This result also follows from (8) where the greatest amplification of any initial perturbation $\boldsymbol{G}_o$ over time t is given by the square root of the maximum eigenvalue [7] of $e^{t\mathbf{A}^\dagger} e^{t\mathbf{A}}$, namely $[\lambda_{\max}(e^{t\mathbf{A}^\dagger} e^{t\mathbf{A}})]^{1/2} = \|e^{t\mathbf{A}}\|$. Any non-defective matrix $\mathbf{A}$ can be decomposed according to the similarity transformation

$$\mathbf{A} \;=\; \mathbf{S}\mathbf{\Lambda}\mathbf{S}^{-1}, \tag{19}$$

where $\mathbf{S}$ is the matrix whose columns are the normalized eigenvectors of $\mathbf{A}$ in order of growth rate and $\mathbf{\Lambda}$ is the diagonal matrix of the associated eigenvalues [15]. This identity can be used to establish bounds on $\|e^{t\mathbf{A}}\|$:

$$\exp(\lambda_{\max} t) \leq \|\exp(t\mathbf{A})\| = \|\mathbf{S}\exp(t\mathbf{\Lambda})\mathbf{S}^{-1}\| \leq \|\mathbf{S}\|\|\mathbf{S}^{-1}\|\exp(\lambda_{\max} t), \tag{20}$$

where $\lambda_{\max}$ is the leading entry of $\mathbf{\Lambda}$. For a normal operator $\mathbf{A}$, $\mathbf{S}$ is unitary, and both the lower and upper bounds on $\|\exp(t\mathbf{A})\|$ equal $\exp(\lambda_{\max} t)\ \forall\ t$. The eigenvalue with largest real part is therefore physically determinant since the growth rate of any disturbance is bounded above by $\lambda_{\max}$, the spectral abscissa of $\mathbf{A}$, which forms the leading entry in $\mathbf{\Lambda}$. For a non-normal operator, the eigenvectors are not orthogonal and the norm of $\mathbf{S}$ and its inverse can be much larger than unity. For highly non-normal systems, several orders of transient amplification can induce nonlinear effects, thereby invalidating the results of modal analysis. The transient behavior of solutions to (13) is therefore determined by examining the time dependence of $\|\exp(t\mathbf{A})\|$. The optimal initial condition that attains the maximum amplification at time t is determined as part of the analysis, which obviates the need to specify an initial form for the perturbation. In these studies, the number of grid points used in discretizing $\mathbf{A}$ ranged from 1600 to 4500; the matrix norms and exponentials were calculated with MATLAB 5.3 [30].

Figure 5 depicts the temporal evolution of $\ln\|\exp(t\mathbf{A})\|$ for selected wavenumbers q. The curves represent the envelopes maximized over all initial conditions of the amplification of individual initial conditions. Initially the system experiences a very small level of transient amplification (small bump near $t = 0$) followed by a brief plateau. By time $t = 5$, the curves with $q \neq 0$ rapidly approach a straight line whose slope equals the eigenvalue predicted from modal analysis. The insignificant level of transient amplification and the rapid convergence to the

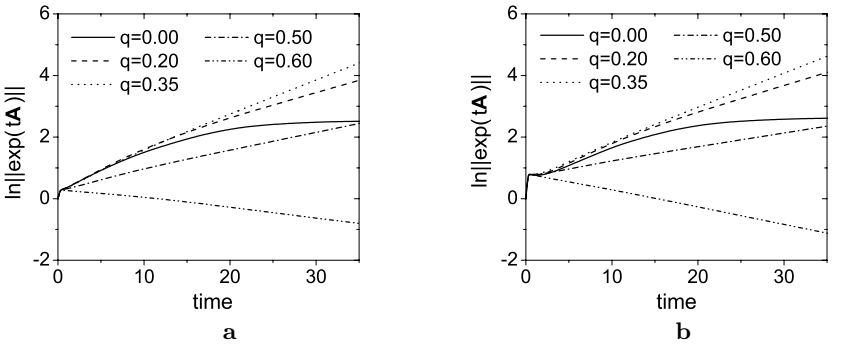

Fig. 5. Maximum possible amplification of disturbances within a time interval t for the height profiles shown in Fig. 1. Parameter values are **a** $\alpha = 0.01$, $\mathsf{C} = 1.0$ and **b** $\alpha = 0.001$, $\mathsf{C} = 0.1$

relevant eigenvalue explains the excellent agreement between experimental measurements of the fingering wavelength and the predictions of the most unstable wavelength from modal theory [21]. The ordering of the wavenumbers according to the degree of amplification level is also identical to the predictions obtained from the eigenspectrum of $\mathbf{A}$. The small degree of transient amplification can be traced to the rather small degree of non-normality of the governing operator, as discussed in Sect. 2.5.

Short Time Behavior. The behavior of the disturbance growth rate in the limit $t \to 0$ is found by expanding the matrix $e^{t\mathbf{A}^\dagger} e^{t\mathbf{A}}$ in (8) in a Taylor series:

$$\lim_{t\to 0} \frac{\mathrm{d}}{\mathrm{d}t} \|e^{t\mathbf{A}}\| \;=\; \lambda_{\max}\left(\frac{(\mathbf{A}+\mathbf{A}^\dagger)}{2}\right). \tag{21}$$

Transient growth occurs when the maximum eigenvalue of the Hermitian part of $\mathbf{A}$ is positive. The structure that experiences the most amplification at early times [7] is the eigenvector associated with the maximum eigenvalue of $(\mathbf{A} + \mathbf{A}^\dagger)/2$. Comparison between this eigenvalue and the slopes of the curves in Fig. 5 as $t \to 0$ provides a check on the numerical computations.

Long Time Behavior. Since $\exp(t\mathbf{A}) = \mathbf{S}\exp(\mathbf{\Lambda}t)\mathbf{S}^{-1}$, the maximum amplification in the limit $t \to \infty$ is dominated exponentially by the first column of $\mathbf{S}$ and the first row of $\mathbf{S}^{-1}$ with amplification factor $\exp[\Re e(\lambda_{\max})t]$. Schwartz's inequality reveals that the normalized initialcondition that produces the maximum growth over time t is the complex conjugate of the first row of $\mathbf{S}^{-1}$, namely $[(\mathbf{S}^{-1})_{r1}]^\dagger$, or the first column of $(\mathbf{S}^\dagger)^{-1}$. Let $\mathbf{S}_L$ denote the matrix whose rows consist of the complex conjugates of the normalized left eigenvectors of $\mathbf{A}$ (the eigenvectors of $\mathbf{A}^\dagger$). By definition, $\mathbf{S}_L\mathbf{S} = \mathbf{I}$, so $\mathbf{S}_L = \mathbf{S}^{-1}$. This relationship implies that the optimal initial condition that undergoes the most amplification as $t \to \infty$ is the first row of $\bar{\mathbf{S}}_L$ (where the overbar denotes the complex conjugate),

which is the leading eigenvector of $\mathbf{A}^\dagger$. The spectral abscissa of $\mathbf{A}$, denoted by $\alpha(\mathbf{A})$, is equal to the growth abscissa, $\gamma(\mathbf{A})$, also known as the Lyapunov exponent [39]:

$$\alpha(\mathbf{A}) \equiv \sup_{z\in\Lambda(\mathbf{A})} \Re e(z) \equiv \Re e[\lambda_{\max}(\mathbf{A})] = \gamma(\mathbf{A}) \equiv \lim_{t\to\infty} t^{-1} \ln \|e^{t\mathbf{A}}\|. \tag{22}$$

As shown in Fig. 5, this asymptotic limit is approached quite early in the spreading process. Evaluation of the time for onset of fingering in various thermocapillary experiments indicates that this asymptotic limit is reached well before the instability is observed [23].

2.5 Pseudospectra

An eigenvalue of a matrix $\mathbf{A}$ is a number $z \in \mathbb{C}$ such that $z\mathbf{I} - \mathbf{A}$ is singular, where $\mathbf{I}$ denotes the identity matrix. Determining the magnitude of the resolvent, $(z\mathbf{I} - \mathbf{A})^{-1}$, for a range of $z \in \mathbb{C}$ provides useful information on the behavior of $\mathbf{A}$ (and the operator of which it is the discrete representation) that cannot be determined by merely computing the eigenvalues. For each $\varepsilon \geq 0$, the ε-pseudospectrum of $\mathbf{A}$ is defined as [39]

$$\Lambda_\varepsilon(\mathbf{A}) \quad = \quad \{z \in \mathbb{C} : \|(z\mathbf{I} - \mathbf{A})^{-1}\| \geq \varepsilon^{-1}\}. \tag{23}$$

If $\mathbf{A}$ is normal then $\Lambda_\varepsilon(\mathbf{A})$ is the union of discs formed by the set of points in $\mathbb{C}$ within a distance ε of the spectrum of $\mathbf{A}$, $\Lambda(\mathbf{A})$. The ε-pseudospectrum may be much larger if $\mathbf{A}$ is non-normal. Examination of plots of $\Lambda_\varepsilon(\mathbf{A})$ gives an indication of the extent of non-normality of a matrix and thus of the physical relevance of its eigenvalues.

The pseudospectra of an operator or matrix can also be used to calculate bounds on $\|\exp(t\mathbf{A})\|$. For each $\varepsilon \geq 0$, the ε-pseudospectral abscissa of $\mathbf{A}$ is defined by

$$\alpha_\varepsilon(\mathbf{A}) \quad = \quad \sup_{z\in\Lambda_\varepsilon(\mathbf{A})} \Re e(z). \tag{24}$$

A lower bound on the norm of the matrix exponential for $\varepsilon > 0$, derived from the Laplace transform, is given by [39]

$$\sup_{t\geq 0} \|\exp(t\mathbf{A})\| \geq \varepsilon^{-1}\alpha_\varepsilon(\mathbf{A}). \tag{25}$$

This bound is relevant if the spectrum is confined to the left halfplane since a lower bound on the transient growth can quickly be found by determining how far the pseudospectra extend into the right halfplane. If the spectrum extends into the right halfplane then this bound is not useful since the growth becomes infinite as $t \to \infty$.

An analogue of the Cauchy integral formula in complex analysis, the Dunford-Taylor integral, provides a representation of any analytic function f of an operator (or matrix) as the integral around an appropriate contour in the complex plane [24]:

$$f(\mathbf{A}) \quad = \quad \frac{1}{2\pi i} \int_\Gamma (z\mathbf{I} - \mathbf{A})^{-1} f(z) dz, \tag{26}$$

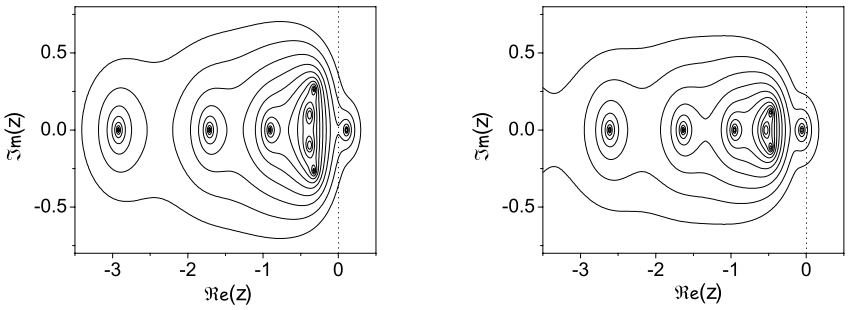

Fig. 6. Plots of the ε-pseudospectra for the base state with $\alpha = 0.001$ and $\mathsf{C} = 0.1$ for wavenumbers **a** $q = 0.35$ and **b** $q = 0.60$. The contours correspond to $\varepsilon = 10^{-1}, 10^{-1.25}, ..., 10^{-3.5}$. The *dotted vertical line* separates the stable and unstable halves of the complex plane

where Γ is any contour enclosing the spectrum of $\mathbf{A}$. Choosing the contour to be the boundary $\partial\Lambda_\varepsilon(\mathbf{A})$ of $\Lambda_\varepsilon(\mathbf{A})$ for some $\varepsilon > 0$ produces an upper bound for the norm of the matrix exponential:

$$\| \exp(t\mathbf{A})\| \leq \frac{1}{2\pi\varepsilon} \int_{\partial\Lambda_\varepsilon(\mathbf{A})} \exp[t\ \Re e(z)]\ |dz|. \tag{27}$$

In practice, this bound is difficult to compute accurately.

Contours of the ε-pseudospectrum were calculated using the Pseudospectra GUI [43] for MATLAB. Boundaries of the ε-pseudospectrum for wavenumbers $q = 0.35$ and $q = 0.60$ for $\alpha = 0.001$ and $\mathsf{C} = 0.1$ are shown in Fig. 6 for a region near the unstable half of the complex plane. The contours shown correspond to values of $\varepsilon = 10^{-1}$, $10^{-1.25}$,..., $10^{-3.5}$. The abscissa and ordinate denote $\Re e(z)$ and $\Im m(z)$, respectively. The curves exhibit only mild non-normality since each contour exceeds the spectrum of $\mathbf{A}$ by an amount only slightly larger than ε, and the eigenvalue with largest real part appears robust. The non-modal amplification is primarily associated with the pairs of complex conjugate eigenvalues near $\Re e(\lambda) \approx -0.5$. The extent of non-normality is even less for larger values of the slip coefficient, which is consistent with the plots of $\ln \| \exp(t\mathbf{A})\|$ vs. t shown in Fig. 5. Although the magnitude of the contact slope (which affects the height of the capillary ridge) influences the eigenvalues found from modal analysis, it has a negligible effect on the level of transient amplification achieved before the modal growth rate is established. Because the contours $\varepsilon \geq 10^{-1.5}$ for $q = 0.60$ extend more than a distance ε beyond the leading eigenvalue and into the unstable section of the complex plane, a small level of transient amplification is expected for this asymptotically stable wavenumber. Applying (25) produces a lower bound on amplification of approximately 1.7, while the actual maximum attained amplification is 2.2, as shown in Fig. 5.

2.6 Optimal Perturbations – SVD

The optimal initial perturbation and its corresponding evolved state at time t are directly computed from the singular value decomposition of $\exp(t\mathbf{A})$ according to [7]

$$\exp(t\mathbf{A}) = \mathbf{U}\boldsymbol{\Sigma}\mathbf{V}^{\dagger}, \tag{28}$$

where the columns of the unitary matrix $\mathbf{V}$ represent the complete set of initial states and the columns of the unitary matrix $\mathbf{U}$ are orthonormal basis vectors that span the range space of final states. The elements, σ_{i}, of the diagonal matrix $\boldsymbol{\Sigma}$ describe the growth realized by each initial state as it is transformed by the propagator into the corresponding final state. Note that the singular value decomposition must be calculated for each time at which $\mathbf{U}$, $\boldsymbol{\Sigma}$, and $\mathbf{V}$ are sought. For an initial perturbation, $\boldsymbol{G}_o = \sum a_{\mathrm{i}}\boldsymbol{V}_{\mathrm{i}}$ with $(\sum |a_{\mathrm{i}}|^2)^{1/2} = 1$, applied at time $t = 0$, the corresponding evolved state at time t is $\boldsymbol{G}(t) = \sum a_{\mathrm{i}}\sigma_{\mathrm{i}}\boldsymbol{U}_{\mathrm{i}} = \exp(t\mathbf{A})\boldsymbol{G}_o$. The vectors $\boldsymbol{V}_{\mathrm{i}}$ are ordered by growth, and the optimal perturbation, $\boldsymbol{V}_{\mathrm{opt}}(t)$, is the initial condition that undergoes the maximum amplification during the interval t. This maximum amplification is denoted by $\sigma_{\max} \equiv \|\exp(t\mathbf{A})\|$ and is given by the leading entry in $\boldsymbol{\Sigma}$.

The maximum possible amplification at any time is attained by the optimal initial disturbance calculated for that time. The normalized evolved state, $\boldsymbol{U}_{\mathrm{opt}}$, corresponding to $\boldsymbol{V}_{\mathrm{opt}}$ evolves into the leading eigenfunction of $\mathbf{A}$, $\boldsymbol{H}(\xi)$, as $t \to \infty$. The optimal initial disturbance, $\boldsymbol{V}_{\mathrm{opt}}(t \to \infty)$, in this long time limit (at which the most unstable mode dominates) asymptotes to $\boldsymbol{H}^{\dagger}(\xi)$, the eigenvector of the adjoint linearized operator, which is the initial condition that optimally excites the most unstable mode, $\boldsymbol{H}(\xi)$.

The excitation for the most asymptotically unstable wavenumber, $q = 0.35$, is plotted in Fig. 7. The disturbance applied at $t = 0$ that elicits the largest

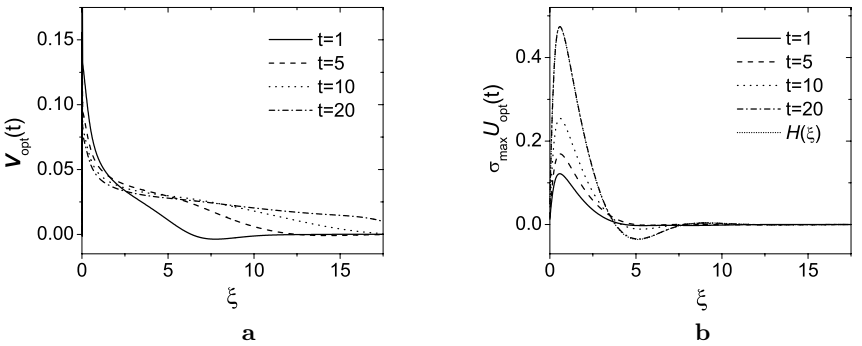

Fig. 7. a Optimal initial disturbance, $\boldsymbol{V}_{\mathrm{opt}}$, and **b** the evolved state, $\sigma_{\max}\boldsymbol{U}_{\mathrm{opt}}$, after time t for a disturbance of wavenumber $q = 0.35$ applied to the base state with $\alpha = 0.10$ and $\mathsf{C} = 0.10$. Each initial disturbance is normalized to unit magnitude. The magnitude of the corresponding evolved state is equal to the amplification attained by the initial disturbance at time t. The evolved state at $t = 20$ cannot be distinguished from the leading eigenfunction, $H(\xi)$

response at $t = 1$ is localized at the contact line. The initial disturbances that undergo the most amplification at later times broaden to encompass much of the capillary ridge but retain maxima at the contact line. Although initially focused near the forward portion of the capillary ridge, the system's response to these perturbations broadens at later times to encompass more of the ridge. By a dimensionless time $t = 15$, this response to the optimal disturbance is nearly indistinguishable from the modal eigenfunction, which explains the excellent agreement between the shape of the eigenfunction and the structure of the experimentally observed instability shortly after onset [21].

2.7 Summary of Thermocapillary Spreading Problem

Because thermally driven liquid films have spatially dependent base states, the linearized disturbance operator, $\mathbf{A}$, is non-normal. The upper bound on disturbance amplification must therefore be determined from the norm of the matrix exponential, $\|\exp(t\mathbf{A})\|$, rather than from the eigenvalue of $\mathbf{A}$ with largest real part, which determines the stability for all time only for normal operators. The transient growth analysis yields several noteworthy results. The ranking of disturbances of wavenumber q from largest to smallest level of disturbance amplification corresponds exactly to the asymptotic results from the modal theory. There is a smooth, rapid transition from the non-modal behavior to the asymptotic results obtained from the eigenspectrum of $\mathbf{A}$. The optimal disturbances for both asymptotically stable and unstable flows initially exhibit a strong peak at the contact line. Disturbances that induce instability rapidly broaden to encompass the entire capillary ridge and the corresponding evolved states rapidly asymptote toward the requisite eigenfunction. The slip boundary condition generates less transient amplification than the use of boundary conditions which predicate a flat [21] or van der Waals precursor film [4] ahead of the contact line, even for very small values of the slip coefficient. This smaller transient growth is caused by the fact that disturbances cannot extend beyond the contact line. For the parameter values examined, the amplification of disturbances is therefore insufficient to trigger nonlinear effects, a conclusion which is reinforced by examination of the pseudospectra of the linearized disturbance operator.

The modal predictions of the slip model and flat precursor film model agree quantitatively if the slip coefficient is equal to the precursor film thickness for an appropriate choice of the contact slope. The dispersion curves for the two models overlap almost exactly for the unstable wavenumbers $q \leq 0.50$. Disturbances in a model employing a structured precursor film governed by van der Waals forces [4] have a slightly smaller growth rate because of the stabilizing influence of attractive van der Waals interactions. All three models predict an identical wavelength for the most unstable disturbance.

The insignificant level of transient amplification and the insensitivity of the asymptotic results to the specific characteristics of the precursor region, combined with the mild non-normality of the linearized disturbance operator, explain the excellent agreement between theory and experiment [23]. Unlike the linearized disturbance operator for plane Poiseuille flow, in which the angle be-

tween the eigenfunctions decreases exponentially as the Reynolds number increases [33], the angle between the eigenfunctions of the leading eigenvalues in thermally driven films is relatively large (63^o in the system studied). This is likely due to the fact that the spatial inhomogeneity of the base state is confined to the capillary ridge. As a result, surface tension, which plays such a critical role in free surface flows, dampens the oscillatory, subdominant modes before significant energy can be transferred to the leading eigenvector. Little transient amplification occurs since the modes interact only weakly.

3 Non-autonomous Operator: Marangoni Spreading from a Finite Surfactant Source

The reduction of (5) to (7) for autonomous operators, which allows straightforward computation of the singular value decomposition of $\| \exp(t\mathbf{A})\|$, is no longer valid for non-autonomous operators. For the Marangoni problem discussed below, there is no reference frame in which the base states can be rendered time-independent. As a result, the disturbance operator $\mathbf{A}$ is non-autonomous. While the singular value decomposition of (5) can still be used to identify the complete set of optimal perturbations ordered by the level of growth realized over a given time interval, numerical implementation of this approach for non-autonomous systems can be formidable, especially for large matrices. In addition, the long time dynamics is not governed by the fastest growing mode but by the Lyapunov vector growing at the mean rate of the first Lyapunov exponent [8]:

$$\lambda = \limsup_{t\to\infty} t^{-1} \ln(\|\mathbf{\Phi}(t)\|). \tag{29}$$

This exponent is analogous to the spectral abscissa in autonomous systems, where $\lambda > 0$ defines asymptotically unstable flow. Information about the associated Lyapunov vector is often much more difficult to obtain than the analogous exercise for autonomous operators which simply reduces to computing the eigenvalues and eigenvectors of $\mathbf{A}$.

Given these difficulties, the Marangoni problem is posed as an initial value problem. Disturbances are applied to selected regions of the flow and their amplification ratio, which is normalized by the temporal behavior of the evolving base state, is monitored in time. Despite this restriction to a limited set of initial conditions, the system of equations is shown to exhibit large transient growth as disturbances ahead of the spreading front convect past the leading edge. Although all the disturbances investigated decay away as $t \to \infty$, the substantial amplification at intermediate times may signal the presence of convective instabilities.

Even for normal operators, care must be taken in defining the stability criterion for time-dependent base states. Shen [36] first introduced the concept of "momentary stability" to describe the situation which prevails at a given instant when the kinetic energy of disturbances diminishes at a faster rate than the kinetic energy of the base state. Likewise, he designated a system "momentarily unstable" if the kinetic energy contained in the disturbance diminishes at

a slower rate than the kinetic energy of the base state. The ratio of the relative energy of the disturbance, $E_d(t)$, to that of the reference (base) state, $E_b(t)$, provides a convenient measure of disturbance growth at time t. Normalizing the energy of the base states and disturbances by the corresponding values at some reference time t_0 leads to the amplification ratio

$$R = \left[\frac{E_d(t)}{E_d(t_o)}\right] / \left[\frac{E_b(t)}{E_b(t_o)}\right] \ , \tag{30}$$

which surveys the intensification or dissipation of the relative input energy for a given time interval. While this definition falls far short of providing the relevant information contained in the first Lyapunov vector and exponent for non-autonomous systems, investigation of the system's response to selected disturbances help pinpoint the critical features of the spreading profile associated with large transient growth.

3.1 Surfactant Driven Flow

Consider a thin incompressible Newtonian liquid film of constant viscosity μ and initial height h_c partially coated with an insoluble surfactant monolayer of length L_c as shown in Fig. 8a. The initial gradient of the spreading pressure, $\Pi = \gamma_o - \gamma_m$ (see Fig. 8b), induces a shear stress $\tau = d\gamma/dx = (d\gamma/d\Gamma)(d\Gamma/dx)$ at the air-liquid interface where Γ is the surface surfactant concentration. Because surface tension is a decreasing function of surfactant concentration, the positive shear stress drives surfactant and liquid toward regions of higher surface tension (uncoated regions). For a finite monolayer source, the driving force $\Pi/L(t)$, where Π is constant, weakens as the monolayer spreads.

The surfactant monolayer is incorporated into the model through the stress boundary condition and the accompanying equation of motion for the surface concentration. This monolayer, however, is regarded as infinitesimally thin such that its surface viscosity and density can be ignored. Furthermore, since the flow is unbounded in the streamwise x-direction, it is assumed that the molecules

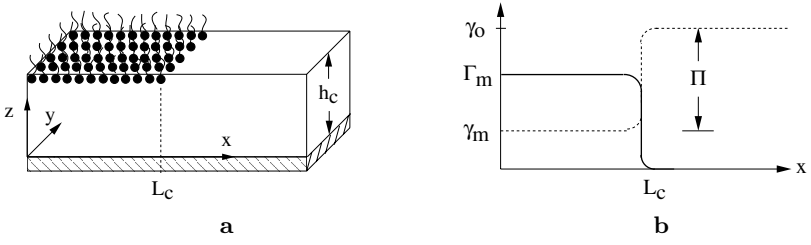

a **b**

Fig. 8. The initial configuration for Marangoni spreading in rectilinear geometry. The liquid layer has viscosity μ, density ϱ, and initial uniform thickness h_c. The initial surfactant monolayer extends a distance L_c with surface tension γ_m and surface concentration Γ_m. The maximum spreading pressure is defined by $\Pi = \gamma_o - \gamma_m$, where the surface tension of the uncoated film is γ_o

comprising the monolayer behave as an ideal gas. The dimensionless equation of state relating the surface tension to the molecular concentration is assumed to be $\gamma = 1 - \Gamma$. Non-linear equations of state have also been studied [9,14].

Within the lubrication approximation [6] and for vanishing Bond number $\varrho g {h_c}^2/\gamma_m$, the dimensionless evolution equations for h and Γ become [20,29]

$$\frac{\partial h}{\partial t} + \nabla \cdot \left(-\frac{h^2}{2} \nabla \Gamma + \frac{\mathcal{C}}{3} h^3 \nabla^3 h \right) = 0 \,, \tag{31a}$$

$$\frac{\partial \Gamma}{\partial t} + \nabla \cdot \left(-\Gamma h \nabla \Gamma + \frac{\mathcal{C}}{2} \Gamma h^2 \nabla^3 h - \frac{1}{Pe_s} \nabla \Gamma \right) = 0 \,. \tag{31b}$$

where the film height is normalized by the initial film thickness h_c, the surfactant concentration by the initial concentration Γ_m, and the streamwise (x) and transverse (y) coordinates by the initial monolayer extent L_c. The dimensionless group $\mathcal{C} = (h_c/L_c)^2 \gamma_m / \Pi$ represents the ratio between the capillary force, which prefers minimal surface area, and the spreading pressure, which is responsible for the increase in surface area. This group can also be written as $\mathcal{C} = (h_c/L_c)^3/Ca$ where $Ca = \mu U_c/\gamma_m$ is the usual capillary number scaled on the characteristic speed, $U_c = (h_c/L_c)\Pi/\mu$, set by the Marangoni stresses. This characteristic speed establishes the convective time scale L_c/U_c used to normalize the dimensional time. The Péclet number $Pe_s = U_c L_c / D_s = \Pi h_c / \mu D_s$ where D_s is the surfactant diffusion coefficient along the surface, represents the ratio between the convective surfactant flux and the diffusive flux. For large Péclet numbers, the diffusive contribution is negligible and the last term in (31b) can be omitted altogether. Returning to (31a), the second and third terms describe the liquid flux contribution from Marangoni stresses and pressure gradients due to surface curvature, respectively. Equation (31b) represents the convective-diffusive transport of surfactant at the air-liquid interface. The second and third terms couple the surfactant concentration to the surface velocity of the spreading film.

3.2 Base State Flow Profiles

In the absence of a constant shear stress, there is no reference frame that renders the spreading process time-independent. It is possible, however, to find a self-similar solution in the limit of infinite capillary number ($\mathcal{C} \to 0$) and infinite Péclet number. In this limit, only Marangoni stresses drive the flow. A straightforward scaling analysis for spreading in rectilinear geometry [20], as in Fig. 8a, reveals that the leading edge of the monolayer advances in time as $t^{1/3}$. The slopes of the film thickness and concentration profiles, however, contain discontinuities which create difficulties in formulating the linear stability analysis [27]. Inclusion of capillarity and surface diffusion destroys the exact self-similar nature of the solutions; however, within the range of parameter values used in this study, the asymptotic profiles approach self-similar form. It is therefore useful to transform the original variables accordingly:

$$\xi = \frac{x}{t^{1/3}} \,, \quad g_o(\xi, t) = t^{1/3} \Gamma_o(x, t) \;\text{ and }\; h_o(\xi, t) = H_o(x, t) \,. \tag{32}$$

The subscript "o" is used to denote the solutions corresponding to the base or unperturbed states. The additional time dependence in the scaling for Γ_o is dictated by the constraint that the total surfactant mass, $\int_0^{L(t)} \Gamma_o(x,t)dx$, remain constant. The dimensionless equations describing the evolution of the film height and surfactant concentration in a frame advancing as $L(t) \sim t^{1/3}$ are given by

$$t\frac{\partial h_o}{\partial t} = \frac{1}{3}\xi h_{o\xi} + \frac{1}{2}\left(h_o^2 g_{o\xi}\right)_\xi - \frac{\mathcal{C}}{3t^{1/3}}\left(h_o^3 h_{o\xi\xi\xi}\right)_\xi , \tag{33a}$$

$$t\frac{\partial g_o}{\partial t} = \frac{1}{3}(\xi g_o)_\xi + \left(g_o h_o g_{o\xi}\right)_\xi - \frac{\mathcal{C}}{2t^{1/3}}\left(g_o h_o^2 h_{o\xi\xi\xi}\right)_\xi + \frac{t^{1/3}}{Pe_s} g_{o\xi\xi} . \tag{33b}$$

The boundary conditions used to solve these equations correspond to symmetry and no-flux of liquid and surfactant at the origin $\xi = 0$ and decay conditions far downstream where the liquid layer is quiescent and free of surfactant:

$$h_{o\xi}(0,t) = 0 , \quad h_{o\xi\xi\xi}(0,t) = 0 \text{ and } g_{o\xi}(0,t) = 0 , \tag{34a}$$

$$h_o(\infty,t) = 1 , \quad h_{o\xi}(\infty,t) = 0 \text{ and } g_o(\infty,t) = 0 . \tag{34b}$$

The initial conditions defined at $t = 1$ correspond to an initially flat liquid layer coated with a surfactant monolayer whose concentration is relatively flat and smoothly decays to zero near the point ξ_o. These two conditions are given by

$$\begin{aligned} h_0(\xi,1) &= 1 \\ g_o(\xi,1) &= {g_o}^{\max} \left[1 - \tanh\left(A(\xi - \xi_o)\right)\right] . \end{aligned} \tag{35}$$

This study was restricted to parameter values ${g_o}^{\max} = 0.5$, $A = 10$, $\xi_o = 0.5$, $\mathcal{C} = 10^{-5}$ and $Pe_s = 5000$. The initial surfactant distribution therefore has an inflection point at ξ_o=0.5 and vanishes at about $\xi = 0.75$, as shown in Fig. 9b. Equations (33a) and (33b) were solved using the method of lines [34], which implements second-order centered differences for the spatial derivatives and a fully implicit Gear's method for the time integration [19]. The number of grid points used in the computations varied between 301 and 751.

Figure 9 depicts the evolution of $h_o(\xi)$ and $g_o(\xi)$ for times $1.0 \leq t \leq 5.0$. As the monolayer spreads along the liquid layer, it shears the underlying liquid film, producing a sharp ridge at the advancing front. Unlike the thermocapillary problem discussed earlier, this ridge is mainly caused by the Marangoni stress which pulls liquid from left to right causing severe thinning near the initial perimeter of surfactant deposition and thickening at the moving front. Capillary forces smooth points of extreme surface curvature, which exist at the apex and thinned portions of the film profile. When capillary and diffusive forces are omitted from the equations, the film thickness (and concentration profile) assumes the shape of a linearly increasing (decreasing) ramp. Behind the apex of the Marangoni ridge, there develops a distinctive linear segment in both h_o and g_o (indicative of the self-similar behavior) which expands in time. As time evolves, $h_o(\xi)$ and $g_o(\xi)$ approach self-similar forms since capillary and diffusive forces weaken considerably with respect to the main driving force.

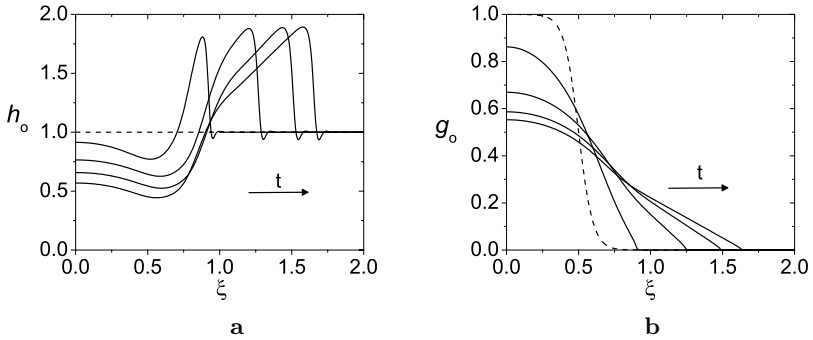

Fig. 9. Evolution of the base state **a** film thickness h_o and **b** surfactant concentration g_o with $Pe_s = 5000$ and $\mathcal{C} = 10^{-5}$ for times $t = 1.0, 1.1, 1.5, 2.6$ and 5.0

Surfactant Compression Effect. It is interesting to examine separately the Marangoni and capillary contributions to the base state surface velocity profile as shown in Fig. 10a for $t = 2.6$. The Marangoni stress causes a sharp increase in the surface speed at the point where the moving film meets the quiescent layer. This increase in speed gives rise to the increase in the film height at the advancing front. The surface tension, acting through the capillary pressure gradient, opposes this motion, causing a negative surface velocity. The combined effect smooths the sharpest features of the velocity profile and introduces a small capillary oscillation just ahead of the monolayer decay point at $\xi \approx 1.5$ to give an overall negative flow speed in this region. This net negative contribution causes a local accumulation of surfactant at the leading edge, which is more easily visualized by examining the gradient in surfactant concentration shown in Fig. 10b. The curve $g_{o\xi}$ decays monotonically away from $\xi = 0$ to reach a minimum at $\xi \approx 0.75$. The gradient plateaus in the region corresponding to the linear por-

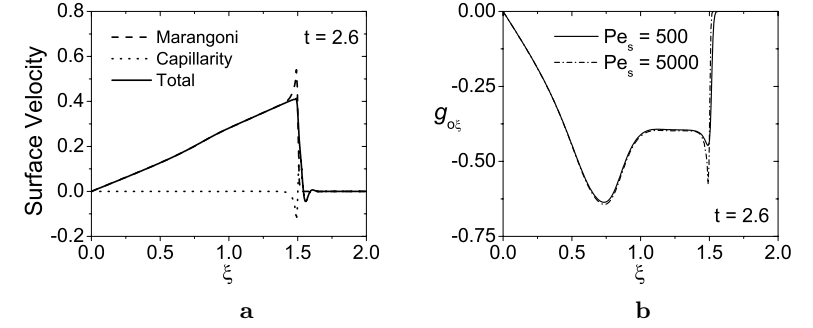

Fig. 10. **a** Marangoni and capillary contributions to the base state surface velocity profile, along with their sum, at time $t = 2.6$ for $Pe_s = 5000$ and $\mathcal{C} = 10^{-5}$. The surface velocity becomes negative just ahead of the step profile. **b** A comparison of $g_{o\xi}$ at time $t = 2.6$ for $Pe_s = 500,\ 5000$ with $\mathcal{C} = 10^{-5}$. The concentration gradient $g_{o\xi}$ undergoes a sharp change at $\xi \approx 1.5$

tions of $h_o(\xi)$ and $g_o(\xi)$ and then sharply falls near the forward midpoint of the Marangoni ridge finally vanishing where the monolayer ends. The local compression of surfactant caused by the capillary pressure at the leading edge causes an increase in the local stress. Decreasing the Péclet number from 5000 to 500, which gives more prominence to surface diffusion, reduces the compression effect as shown in Fig. 10b. In physical systems, this compression effect is always present if the spreading is dominated by Marangoni forces.

At $t = 2.6$, the shear stress is largest near $\xi = 0.75$ since this is the region that suffers the most rapid change in surface tension as the spreading begins. A similar effect occurs at the leading edge of the surfactant monolayer since the local accumulation of surfactant causes a local enhancement in the concentration gradient. It is expected that these two critical regions, which experience the largest shear stress, are particularly vulnerable to disturbances. This issue is discussed further in Sect. 3.3.

3.3 Linear Stability of Time Dependent Base State Profiles

The stability of infinitesimal disturbances to the film thickness and surfactant concentration with sinusoidal variations in the transverse direction ($\hat{y}$) are investigated next. The perturbed waveforms are defined by $h(x,y,t) = h_o(x,t) + \varepsilon\widetilde{H}(x,y,t)$ and $\Gamma(x,y,t) = \Gamma_0(x,t) + \varepsilon\widetilde{\Gamma}(x,y,t)$ ($\varepsilon \ll 1$), where

$$(\widetilde{H},\widetilde{\Gamma})(x,y,t) = (\Psi,\Phi)(x,t)e^{iqy}\,. \tag{36}$$

The dimensionless wavenumber q, normalized by L_c, is associated with the transverse corrugations, which are denoted by a tilde. With this choice, disturbances to the film height and surfactant concentration are applied in phase. Other choices are possible. The Fourier amplitudes, Ψ and Φ, are further rescaled by transforming to the moving reference frame of the base states as in (32):

$$\Psi(x,t) = \psi(\xi,t) \quad \text{and} \quad \Phi(x,t) = \frac{\phi(\xi,t)}{t^{1/3}}\,. \tag{37}$$

Substitution of these equations into (31a) and (31b) leads to the linearized set of equations for the evolution of the disturbance film thickness, $\psi(\xi,t)$, and the disturbance concentration field, $\phi(\xi,t)$ [28]:

$$\begin{aligned} t\frac{\partial\psi}{\partial t} &= \frac{1}{3}\xi\psi_\xi + \frac{1}{2}\left({h_o}^2\phi_\xi + 2h_o g_{o\xi}\psi\right)_\xi - \frac{(qt^{1/3})^2}{2}{h_o}^2\phi \\ &\quad - \frac{\mathcal{C}}{3t^{1/3}}\left[\left({h_o}^3\psi_{\xi\xi\xi} + 3{h_o}^2 h_{o\xi\xi\xi}\psi\right)_\xi\right. \\ &\quad \left. - (qt^{1/3})^2\left(({h_o}^3)_\xi\psi_\xi + 2{h_o}^3\psi_{\xi\xi}\right) + (qt^{1/3})^4{h_o}^3\psi\right]\,, \qquad (38a) \\ t\frac{\partial\phi}{\partial t} &= \frac{1}{3}(\xi\phi)_\xi + \left(g_o g_{o\xi}\psi + h_o g_{o\xi}\phi + h_o g_o\phi_\xi\right)_\xi - (qt^{1/3})^2 h_o g_o\phi \\ &\quad - \frac{\mathcal{C}}{2t^{1/3}}\left[\left(g_o{h_o}^2\psi_{\xi\xi\xi} + 2g_o h_o h_{o\xi\xi\xi}\psi + {h_o}^2 h_{o\xi\xi\xi}\phi\right)_\xi\right. \end{aligned}$$

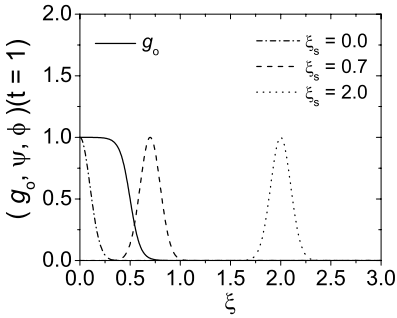

Fig. 11. Three locations of the initial perturbations, $\psi(t=1)$ and $\phi(t=1)$, relative to the initial base state concentration profile $g_o(t=1)$

$$- \left(qt^{1/3}\right)^2 \left((g_o {h_o}^2)_\xi \psi_\xi + 2 g_o {h_o}^2 \psi_{\xi\xi} \right) + \left(qt^{1/3}\right)^4 g_o {h_o}^2 \psi \Big]$$
$$+ \frac{t^{1/3}}{Pe_s} \left[\phi_{\xi\xi} - \left(qt^{1/3}\right)^2 \phi \right] \ . \tag{38b}$$

Similar boundary conditions used for solving the base state equations are applied to the disturbance equations, namely:

$$\psi_\xi(0,t) = 0 \ , \quad \psi_{\xi\xi\xi}(0,t) = 0 \ , \quad \text{and} \quad \phi_\xi(0,t) = 0 \ , \tag{39a}$$
$$\psi(\infty,t) = 0 \ , \quad \psi_\xi(\infty,t) = 0 \ , \quad \text{and} \quad \phi(\infty,t) = 0 \ . \tag{39b}$$

The initial conditions chosen for this study represent highly localized Gaussian functions that are positioned either well ahead of the initial monolayer front ($\xi_s = 2.0$), at the base of the initial monolayer perimeter ($\xi_s = 0.7$), or at the origin ($\xi_s = 0.0$). These disturbances are described by:

$$\psi(\xi,1) = \phi(\xi,1) = \ e^{-\mathrm{B}\,(\xi-\xi_s)^2} \ . \tag{40}$$

The amplitudes $\psi(\xi,1)$ and $\phi(\xi,1)$ are set to unity since (38a) and (38b) are linear equations. In this study, $B = 50$. Figure 11 shows three locations of the Gaussian perturbations chosen for this study.

Equations (33a), (33b), (38a) and (38b) are solved simultaneously using the method of lines as described earlier. Equations (33a) and (33b) are discretized and cast into the operator form (2) by defining state vectors $\boldsymbol{G} = [\psi \ \phi]$. Since there exists both an implicit and explicit time dependence in (38a) and (38b), the linearized operator $\mathbf{A}$ is non-autonomous; the generalized stability analysis described in Sect. 1.2 can therefore be invoked. An alternative, less general approach is used below for computational expedience. Gaussian distributed perturbations in the film thickness and surfactant concentration are positioned at key points in the spreading film. This targeted approach uncovers at least one region of the flow which is particularly vulnerable to disturbance growth.

3.4 Transient Growth Analysis

The amplification ratio defined by (30) requires specification of the quantity to be used in monitoring the production and dissipation of energy. Previous studies of centrifugal and thermocapillary spreading adopted the quantity, $h^2(\boldsymbol{x},t)$, which is proportional to the kinetic energy associated with the dominant driving force [21,22,37] (but not precisely equal to the kinetic energy). For Marangoni driven spreading the flow speed is determined by the coupling of the film height to the surfactant concentration gradient. The height averaged kinetic energy of the flow per unit wavelength, $\lambda = 2\pi/q$, is given by:

$$E_b \equiv \frac{1}{2\lambda}\int_0^{\lambda}\int_0^{\infty} |\langle \boldsymbol{v_o}\rangle|^2 d\xi dy \qquad \text{and} \qquad E_d \equiv \frac{1}{2\lambda}\int_0^{\lambda}\int_0^{\infty} |\langle \widetilde{\boldsymbol{v}}\rangle|^2 d\xi dy \; . \tag{41}$$

where the subscripts b and d denote the base state and disturbance, respectively. The magnitude of the base state velocity vector is given by $|\langle \boldsymbol{v_o}\rangle|$ and that of the disturbance velocity field by $|\langle \widetilde{\boldsymbol{v}}\rangle|$, with height averaged quantities denoted by angular brackets. The height-averaged base state velocity fields in the streamwise and transverse directions (the vertical component is negligible within the lubrication approximation) are given by

$$\begin{aligned} \langle u_o\rangle &= -\frac{1}{2t^{2/3}} h_o g_{o\xi} + \frac{\mathcal{C}}{3t} {h_o}^2 h_{o\xi\xi\xi} \; , \\ \langle w_o\rangle &= 0 \; , \end{aligned} \tag{42}$$

respectively, while those of the averaged disturbance velocities are given by

$$\begin{aligned} \langle \widetilde{u}\rangle &= \left[-\frac{1}{2t^{2/3}} \left(h_o \phi_\xi + g_{o\xi}\psi \right) + \frac{\mathcal{C}}{3t} h_o \left(h_o \psi_{\xi\xi\xi} + 2h_{o\xi\xi\xi}\psi - t^{2/3} q^2 h_o \psi_\xi \right) \right] e^{iqy} \; , \\ \langle \widetilde{w}\rangle &= \left[-\frac{1}{2t^{1/3}} q h_o \phi + \frac{\mathcal{C}}{3t^{2/3}} q {h_o}^2 \left(\psi_{\xi\xi} - t^{2/3} q^2 \psi \right) \right] i e^{iqy} \; . \end{aligned} \tag{43}$$

3.5 Mechanism for Large Transient Growth

Depending on the initial location ξ_s of the applied disturbances, the system undergoes different levels of amplification as shown in Fig. 12. When disturbances are applied at the origin (well inside the monolayer), the amplification ratio R rapidly decays from one to zero (Fig. 12a). The decay is more rapid for larger wavenumbers. The shear stress near the origin is very small and flow is not vulnerable to disturbance amplification.

For disturbances applied further downstream at $\xi_s = 0.7$, near the base of the initial concentration decay point, the system undergoes a brief period of small transient growth. Figure 12b shows that the smallest wavenumbers experience the largest amplification. The mode with $q = 0$ achieves an overall amplification ratio of about 25 and slowly decays toward zero as $t \to \infty$. Despite this short lived boost, disturbances with $q \neq 0$ dissipate their energy by $t \approx 1.5$. Additional studies of the rate of change $R^{-1}dR/dt$ has led to the following interpretation

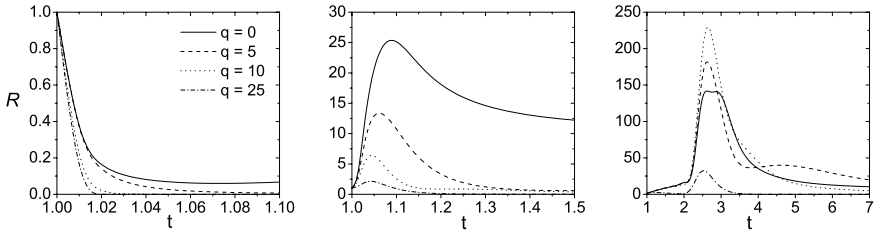

Fig. 12. Time evolution of the amplification ratio for **a** $\xi_s = 0.0$, **b** $\xi_s = 0.7$, and **c** $\xi_s = 2.0$ with disturbance wavenumbers in the range $0 \leq q \leq 25$ for $Pe_s = 5000$ and $\mathcal{C} = 10^{-5}$

of the flow [9]. When a disturbance is first applied to the spreading film, the system counteracts the disturbance flow by establishing Marangoni and capillary pressure gradients in the transverse direction ($\hat{y}$) that drive liquid and surfactant away from the disturbance to produce a momentary stabilizing response. The system overshoots this response, however, giving rise to an enhanced streamwise flow that produces the maximum in R shown for each curve. Eventually, the Marangoni stresses die away and therefore so does the driving force for spreading. In the limit $t \to \infty$ all disturbances decay to zero.

Significant amplification occurs when the initial disturbance is applied well ahead of the initial monolayer at ξ_s=2.0 (see Fig. 12c). In this case, the base state has sufficient time to develop a sizeable Marangoni ridge, which enhances the mobility of the disturbance when the two meet. The amplification therefore occurs at a later time in the spreading process (cf. Fig. 12b,c). Not only are the amplification ratios almost an order of magnitude larger but the duration of the enhanced response is also much longer. Because the speed of the advancing front decays in time as $dL/dt \sim t^{-2/3}$, the disturbance has a longer residence time in the vicinity of the Marangoni ridge than is the case with disturbances localized further upstream. The mode with the largest overall R also switches from $q = 0$ to $q = 10$ with successively smaller enhancement for $q = 5, 0$ and 25 in that order. There is an additional interesting difference between Figs. 12b and 12c. While in Fig. 12b the small q modes attain their maximum amplification ratio at later times than the large q disturbances, Fig. 12c shows that all the wavenumbers resonate at approximately the same time.

A recent study has revealed that the location of applied disturbances has a significant effect on which mode undergoes the strongest amplification [9] as shown in Table 1. Specifically, the $q = 0$ mode undergoes the largest transient growth when disturbances are localized at or behind the initial concentration distribution. By contrast, disturbances placed farther downstream selectively promote the $q = 10$ mode.

Table 1. Wavenumbers yielding the largest amplification ratio for different disturbance locations when $Pe_s = 5000$ and $\mathcal{C} = 10^{-5}$

ξ_s	0.0	0.7	1.0	1.5	1.7	2.0
$q_{\max}$	0	0	0	10	10	10

3.6 Summary of Marangoni Driven Spreading

The disturbance functions, $\psi(\xi, t)$ and $\phi(\xi, t)$, corresponding to $q = 10$ and $\xi_s = 2.0$ are plotted in Fig. 13 for times $t = 1.0, 2.6$ and 8.0. In comparing these curves to the base state profiles shown in Figs. 9 and 10b, it is evident that the largest transient response occurs when the disturbances migrate to the point where the concentration gradient undergoes the most rapid change (*i.e.* the region of surfactant compression discussed earlier), which is also a region of high curvature in film thickness. For the case shown, the maximum amplification occurs at $\xi = 1.5$ for $t = 2.6$. A second region of large shear stress at $\xi = 0.7$ is not as vulnerable to disturbances since R, $\psi(\xi, t)$ and $\phi(\xi, t)$ rapidly decay for $t > 3.0$ for $\xi_s = 2.0$. It is likely that these disturbances are stabilized by the much slower base flow speed in this region. A comparison of Figs. 9a, 13a, and 10b indicates that as the disturbance functions advect through the Marangoni ridge into the linear portion of the height profile (where the concentration gradient is constant), the amplification ratio approaches zero. Increasing the level of surface diffusion by decreasing Pe_s leads to a substantial decrease in amplification. For example, disturbances with $q = 10$ initially localized well ahead of the spreading front suffer a reduction in the maximum value of R from approximately 230 to 15 as Pe_s is decreased from 5000 to 100. Values of Pe_s in experiments are estimated to be closer to 5000.

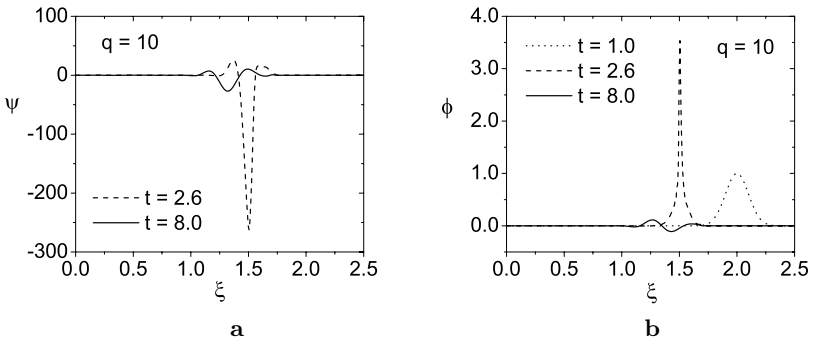

Fig. 13. Solutions for the disturbances in **a** film thickness, ψ, and **b** surfactant concentration, ϕ, for times ranging from $1.0 \leq t \leq 8.0$ with $q = 10$ and $\xi_s = 2.0$. The amplitude of the function $\psi(\xi, t = 1)$ in **a** is too small to be visible

Additional studies have shown that the decay rate of disturbances with $q > 10$ is even more rapid. For $q = 25$, the disturbance functions die away completely before they are convected into the linear regions of the base state profiles. As shown in Fig. 12c, disturbances with $q = 0$ also undergo significant amplification. Interestingly, the functions $\psi(\xi, t)$ and $\phi(\xi, t)$ assume shapes almost identical to $h_{o\xi}$ and $g_{o\xi}$. This equivalence cannot be derived analytically from (38a) and (38b). The equivalence between the disturbance eigenfunction $G(\xi)$ and the first spatial derivative of the base state $h_\xi(\xi)$ can be derived analytically for the time-independent equations governing gravitationally driven [40] or thermocapillary driven films [21].

The analysis presented above, which reduces the original stability analysis of a non-autonomous, non-normal system to a simpler initial value problem prevents identification of the optimal perturbations. It nonetheless provides valuable insight into possible mechanisms for instability. Because both the perturbations and the base states evolve in time, however, the energy growth of perturbations must be measured relative to that of the evolving base states. For a finite monolayer spreading over a thin liquid film, the analysis identifies the leading edge of the spreading front, where $h_{o\xi\xi}$ and $g_{o\xi\xi}$ are particularly large, as the region most susceptible to disturbance amplification.

Table (1) indicates that disturbances with $q = 10$ undergo the largest amplification if placed ahead of the initial surfactant monolayer. This placement allows development of a significant Marangoni ridge that amplifies disturbances upon contact. This prediction of a selective wavenumber is encouraging because it is one aspect of the instability that can be measured and compared with experiment. Experimental evidence, however, has not demonstrated whether the observed fingering patterns are an asymptotic instability or a nonlinear instability triggered by nonlinear mechanisms. The fact that all the localized disturbances investigated vanish as $t \to \infty$ predicts that the system is asymptotically stable. This asymptotic decay, however, is likely due to the fact that in these studies, the overall mass of surfactant contained in the source region is rather small. Current studies [10,11] clearly show that surfactant distribution from a more massive source than considered in Sect. 3.2 (modeled either as a large and fixed concentration at the origin or as a time-dependent release) generates more pronounced film thinning behind the advancing front with a consequent bottleneck for surface transport. This bottleneck leads to rapid disturbance localization and sufficient sustained amplification to produce asymptotic instability.

4 Conclusion

The presence of a deformable free surface in thin films driven to spread by body or shear forces gives rise to base states that are spatially nonuniform. This nonuniformity produces linearized disturbance operators that are non-normal and an eigenspectrum that may not be physically determinant at finite times. In this article, two examples of free surface shear flows are investigated, namely thermocapillary and Marangoni driven spreading. The first involves driving the coating

flow with a constant shear stress that is induced by a streamwise linear temperature profile. The second involves spreading driven by a non-constant shear stress that is caused by an insoluble surfactant monolayer with non-uniform distribution. The associated disturbance operator for the thermocapillary system is autonomous but non-normal. This example is therefore used to demonstrate a more generalized, rigorous non-modal approach to linear stability for free surface flows. Calculations of the maximum disturbance amplification and the pseudospectra for this system, however, reveal weak non-normality and transient growth such that the modal growth rate is rapidly recovered. Subdominant modes contribute little energy to the leading eigenvector because their oscillatory behavior is rapidly damped by surface tension. Generalization of these results to numerous other lubrication flows involving surface tension and a constant driving force may suggest similarly weak non-normality and transient growth.

The base states corresponding to a finite monolayer spreading on a thin viscous film do not support constant traveling wave solutions. The film thickness and concentration profiles are rather complex waveforms, each with distinctive features that advance at different rates. Of particular interest are two regions of the flow profile where the gradient in shear stress and film curvature is large - namely, the region just ahead of the decay point of the initial surfactant distribution and a region at the leading edge of the spreading film where capillary forces produce surfactant compression. The disturbance operator for this system is non-autonomous and highly non-normal. Although the formalism for generalized linear stability outlined in Sect. 1.2 is applicable to non-autonomous operators, the disturbance propagator is difficult to compute accurately because the evolving base states and disturbance functions must be numerically evaluated in time. This universal approach to linear stability is therefore not applied to the Marangoni spreading problem. The analysis is instead reduced to an initial value problem to provide information about the physical mechanisms driving the observed instability. Initial disturbances are localized to various positions along the spreading profile to help determine the source of the transient disturbance growth. Disturbances initially localized well ahead of the surfactant monolayer undergo amplification by over two orders of magnitude (for the parameters used in this study). This amplification is traced to the leading edge of the Marangoni ridge where the second derivative of the surfactant concentration is particularly large, as is the curvature of the liquid surface.

An interesting avenue for further investigation is the application of successive excitations to the base states by sequential perturbations ahead of the advancing front. Such perturbations could maintain a large disturbance amplification ratio, increasing the potential for non-linear effects. A full nonlinear analysis of the response to such initial perturbations would be needed to ascertain if these effects can produce the requisite destabilization. Although the energy analysis has isolated a region in the flow that is most susceptible to disturbances and an associated preferred wavelength for large transient growth, direct comparison to experiment remains elusive since it is difficult to excite infinitesimal disturbances of specified shape. In contrast to thermocapillary spreading, little quantitative experimental data exists for Marangoni spreading. Additional theoretical and

experiment work is required to understand fully the intricate arterial patterns observed experimentally.

Acknowledgment

We kindly acknowledge funding from the National Science Foundation (CTS and DMR), Unilever Research US and NASA Fluid Physics in support of our ongoing studies of thin film flows and hydrodynamic instabilities. JMD also wishes to thank the Department of Defense for a National Defense Science and Engineering Graduate Fellowship.

References

1. A.W. Adamson: *Physical Chemistry of Surfaces*, (John Wiley & Sons, New York 1990)
2. S. Chandrasekhar: *Hydrodynamic and Hydromagnetic Stability*, (Dover Publications, Inc., New York 1961)
3. J.M. Davis, S.M. Troian: "Influence of Boundary Slip on the Optimal Excitations in Thermally Driven Spreading," in review for Phys. Rev. E (2002)
4. J.M. Davis, S.M. Troian: Phys. Rev. E **67**, 016308:1-9 (2003)
5. J.M. Davis, S.M. Troian: Phys. Fluids **15**, 1344 (2003)
6. W.M. Deen: *Analysis of Transport Phenomena*, (Oxford University Press, New York 1998)
7. B.F. Farrell, P.J. Ioannou: J. Atmos. Sci. **53**, 2025 (1996)
8. B.F. Farrell, P.J. Ioannou: J. Atmos. Sci. **53**, 2041 (1996)
9. B.J. Fischer, S.M. Troian: Phys. Rev. E **67**, 016309:1-11 (2003)
10. B.J. Fischer, S.M. Troian: "Thinning and Disturbance Growth in Liquid Films Mobilized by Continuous Surfactant Delivery", in press for Phys. Fluids (2003)
11. B.J. Fischer, S.M. Troian: "The Linear Stability of Thin Films Subject to a Sharp Change in Shear Stress", submitted to Langmuir (2003)
12. N. Fraysse, G.M. Homsy: Phys. Fluids **6**, 1491 (1994)
13. F.R. Gantmacher: *The Theory of Matrices*, vol. 2. (Chelsea Publishing Company, New York 1964)
14. D.P. Gaver, J.B. Grotberg: J. Fluid Mech. **213**, 127 (1990)
15. G.H. Golub, C.F. Van Loan: *Matrix Computations*, 2nd ed. (Johns Hopkins University Press, Baltimore, MD 1990)
16. H. Greenspan: J. Fluid Mech. **84**, 125 (1978)
17. C. Huh, L.E. Scriven: J. Colloid Interface Sci. **35**, 85 (1971)
18. H.E. Huppert: Nature **300**, 427 (1982)
19. A.C. Hindmarsh: 'ODEPACK - A systemized collection of ODE solvers'. In: *Scientific Computing*, ed. by R. S. Stepleman, (North-Holland, Amsterdam 1983) pp. 55
20. O.E. Jensen, J.B. Grotberg: J. Fluid Mech. **240**, 259 (1992)
21. D.E. Kataoka, S.M. Troian: J. Colloid Interface Sci. **192**, 350 (1997)
22. D.E. Kataoka, S.M. Troian: J. Colloid Interface Sci. **203**, 335 (1998)
23. D.E. Kataoka: The Spreading Behavior of Thermally Driven Liquid Films. Ph.D. Thesis, Princeton University, Princeton (1999)
24. T. Kato: *Perturbation Theory for Linear Operators*, (Springer-Verlag, New York 1966)

25. V.G. Levich: *Physicochemical Hydrodynamics*, (Prentice-Hall, Englewood Cliffs 1962)
26. V. Ludviksson, E.N. Lightfoot: AIChE Journal **17**, 1166 (1971)
27. O.K. Matar, S.M. Troian: Phys. Fluids **10**, 1234 (1998)
28. O.K. Matar: The Dynamic Behavior of an Insoluble Surfactant Monolayer Spreading on a Thin Liquid Film. Ph.D. Thesis, Princeton University, Princeton, NJ (1998)
29. O.K. Matar, S.M. Troian: Phys. Fluids **11**, 3232 (1999)
30. *MATLAB 5.3*, (The MathWorks Inc., Natick, MA, 1999)
31. F. Melo, J.F. Joanny, S. Fauve: Phys. Rev. Lett. **63**, 1958 (1989)
32. A. Oron, S.H. Davis, S.G. Bankoff: Rev. Mod. Phys. **69**, 931 (1997)
33. S.C. Reddy, P.J. Schmid, D.S. Henningson: SIAM J. Appl. Math. **53**, 15 (1993)
34. W.E. Schiesser: *The Numerical Method of Lines*, (Academic Press, San Diego 1991)
35. P.J. Schmid, D.S. Henningson: *Stability and Transition in Shear Flows*, (Springer-Verlag, New York 2001)
36. S.F. Shen: J. Aerospace Sci. **28**, 397 (1961)
37. M.A. Spaid, G.M. Homsy: Phys. Fluids **8**, 460 (1996)
38. L.N. Trefethen, A.E. Trefethen, S.C. Reddy, T.A. Driscoll: Science **261**, 578 (1993)
39. L.N. Trefethen: SIAM Rev. **39**, 383 (1997)
40. S.M. Troian, E. Herbolzheimer, S.A. Safran, J. F. Joanny: Europhys. Lett. **10**, 25 (1989)
41. S.M. Troian, X.L. Wu, S. A. Safran: Phys. Rev. Lett. **62**, 1496 (1989)
42. S.M. Troian, E. Herbolzheimer, S.A. Safran: Phys. Rev. Lett. **65**, 333 (1990)
43. T.G. Wright, L.N. Trefethen: SIAM J. Sci. Comp. **23**, 591 (2001)